Ongoing Westward Migration of Drainage Divides in 1 Eastern Tibet, Quantified from Topographic Analysis

Chao Zhou[1], Xi-Bin Tan[2], and Yiduo Liu[3]

[1]Institute of Geology
[2]Institute of Geology, China Earthquake Administration
[3]University of Houston

November 25, 2022

Abstract

Landscape evolution is controlled by tectonic strain, bedrock lithology, and climatic conditions, and is expressed in the spatial and temporal variations in river channel networks. In response to tectonic and climatic disturbance, river networks shift both laterally and vertically to achieve a steady state. Several metrics are available to assess the nature of river network disequilibrium, upon which the direction of drainage divide migration can be interpreted. However, to link this information to other observational, theoretical, and experimental data requires the knowledge of the rate of migration, which is still lacking. Here we develop a modified method based on Gilbert metrics to calculate the transient direction and rate of drainage divide migration from topography. By choosing a high base level, linear or quasi-linear χ-plots are obtained for rivers on both sides of the drainage divide, and the elevation-χ gradient is proportional to the average normalized steepness index (ksn). In turn, the velocity of divide migration can be quantified theoretically from the cross-divide comparison of χ. We applied this method to eastern Tibet and obtained a uniform, westward migration pattern for 29 points along two drainage divides with rates between 0.02 and 0.66 mm/yr, which is consistent with the great river capture events in the region. The ongoing reorganization of the river network in eastern Tibet is caused by the Cenozoic growth and eastward expansion of the Tibetan Plateau, the strengthening of the precipitation and regional extension throughout East Asia, and the local fault activities.

Ongoing Westward Migration of Drainage Divides in Eastern Tibet, Quantified from Topographic Analysis

Chao Zhou[1, 2], Xibin Tan[1, 2, *], Yiduo Liu[3, *], Renqi Lu[1, 2], Michael A. Murphy[3], Honglin He[1, 2], Zhujun Han[1], Xiwei Xu[4]

[1] State Key Laboratory of Earthquake Dynamics, Institute of Geology, China Earthquake Administration, Beijing 100029, China

[2] Shanxi Taiyuan Continental Rift Dynamics National Observation and Research Station, Beijing, 100029, China

[3] Department of Earth and Atmospheric Sciences, University of Houston, Houston, TX 77204-5007, USA

[4] National Institute of Natural Hazards, Beijing, 100085, China

*Corresponding author: tanxibin@ies.ac.cn (X. Tan); yliu54@central.uh.edu (Y. Liu)

Abstract

Landscape evolution is controlled by tectonic strain, bedrock lithology, and climatic conditions, and is expressed in the spatial and temporal variations in river channel networks. In response to tectonic and climatic disturbance, river networks shift both laterally and vertically to achieve a steady state. Several metrics are available to assess the nature of river network disequilibrium, upon which the direction of drainage divide migration can be interpreted. However, to link this information to other observational, theoretical, and experimental data requires the knowledge of the rate of migration, which is still lacking. Here we develop a modified method based on Gilbert metrics to calculate the transient *direction and rate* of drainage divide migration from topography. By choosing a high base level, linear or quasi-linear χ-plots are obtained for rivers on both sides of the drainage divide, and the elevation-χ gradient is proportional to the average normalized steepness index (k_{sn}). In turn, the velocity of divide migration can be quantified theoretically from the cross-divide comparison of χ. We applied this method to eastern Tibet and obtained a uniform, westward migration pattern for 29 points along two drainage divides with rates between 0.02 and 0.66 mm/yr, which is consistent with the great river capture events in the region. The ongoing reorganization of the river network in eastern Tibet is caused by the Cenozoic growth and eastward expansion of the Tibetan Plateau, the strengthening of the precipitation and regional extension throughout East Asia, and the local fault activities.

Keywords:

Divide migration rate; Chi-plot; Channel steepness; Longmen Shan; Eastern Tibet

1. Introduction

Landscape evolution is controlled by the development and organization of drainage basins, which is fundamentally controlled by tectonics, lithology, and climatic conditions (Molnar and England, 1990; Whipple, 2009; Zondervan et al., 2020). Geomorphic parameters are widely used to reconstruct past tectonic (e.g., Kirby et al., 2003; Forte et al., 2015; Shi et al., 2021) and climatic processes (e.g., Tucker and Slingerland, 1997; Nie et al., 2018). Tectonic and climate disturbances drive drainage divides to migrate, which impacts river incision by changing the drainage area (Whipple et al., 2017; Vacherat et al., 2018; Yang et al., 2020) and can further influence crustal deformation (Steer et al., 2014; Tan et al., 2018; Liu et al., 2020). Quantitatively measuring the divide migration rate, therefore, is desired as it will not only promote the tectonic and climatic information extraction from topography, but also provide key information for biodiversity conservation (Rahbek et al., 2019).

Drainage divide migration is essentially driven by the cross-divide differential erosion (Willett et al., 2014; Forte and Whipple, 2018; Dahlquist et al., 2018; Hu et al., 2021). Cross-divide erosion rates are routinely derived from geochronological techniques, such as cosmogenic ^{10}Be dating, which have been used to calculate the divide migration rate (Beeson et al., 2017; Hu et al., 2021). Such techniques are usually based on samples collected from the outlet of a few selected drainage basins and may not represent the erosion rates close to the drainage divide as a whole. Ideally, it is necessary to find a cost-effective method that can be applied to the entire landscape, to cross-check and make full use of the cosmogenic ages. Forte and Whipple (2018) suggested that the cross-divide difference in erosion rate is driven by the cross-divide difference in topographic gradient. The “Gilbert” metrics include the cross-divide difference in channel elevation at a reference drainage area, mean headwater hillslope gradient, and mean headwater local relief and are proposed to judge the stability of drainage divides (Whipple et al., 2017; Forte and Whipple, 2018). However, the erosion rate is affected not only by the topographic gradient, but also by the upstream drainage area, precipitation, and lithology (Howard, 1994; Whipple and Tucker, 1999; Kirby and Whipple, 2012). Therefore, one still cannot obtain the migration rate from the conventional Gilbert metrics. The normalized channel steepness (k_{sn}) is a more reliable and widely-used metric than topographic gradient to reveal erosion rate (Kirby et al., 2001; Wobus et al., 2006; Kirby and Whipple, 2012). In theory, the cross-divide comparison on k_{sn} could be used to quantify the divide migration rate. However, this technique has only been used to judge the direction of drainage divide migration so far (He et al., 2019; Chen et al., 2021).

In this study, we develop a new method modified from the Gilbert metrics to extract the transient divide migration *direction and rate* from topography. We firstly derive an equation for the relationship between the normalized cross-divide differences in erosion rate ($\Delta E/\bar{E}$) and χ ratio (χ_α/χ_β). Then we calculate the top-most χ-plots with high base levels in the eastern Tibetan river network, and obtain the normalized differences in erosion rate based on the equation. We further calculate the divide migration rates based upon the topographic slopes of both sides and the measured or estimated erosion rates. The new formula enables us to map the velocity of drainage divide migration, evaluate the driving mechanisms (Shi et al., 2021), and explores the interactions among various processes in the Earth system (Molnar and England, 1990; Nie et al., 2018).

2. Method

The longitudinal profile of a river records information on bedrock lithology, tectonic strain, and climate history. According to the detachment-limited stream power model (Howard, 1994), the erosion rate, E, is usually expressed in terms of channel gradient, S, and drainage area, A:

$$E = KA^m S^n \tag{1}$$

or a transformed expression:

$$S = \left(\frac{E}{K}\right)^{\frac{1}{n}} A^{\frac{-m}{n}} \tag{2}$$

where K is a dimensional coefficient of erosion, and m and n are positive constants that are referred to as area exponent and slope exponent, respectively (Whipple and Tucker, 1999; Kirby and Whipple, 2012). A river longitudinal elevation (z) profile can be expressed by integration in the upstream direction from a base x_b to an observation point x:

$$z(x) = z_b + \int_{x_b}^{x} \left(\frac{E(x)}{K(x)}\right)^{\frac{1}{n}} A(x)^{\frac{-m}{n}} dx \tag{3}$$

where z_b is the elevation at the river network's base level at $x = x_b$. In the case of spatially invariant erosion rate (E) and erosion coefficient (K), Eq. (3) can be reduced to a simpler form:

$$z(x) = z_b + k_{sn}(A_0)^{\frac{-m}{n}}\chi \tag{4}$$

with

$$k_{sn} = \left(\frac{E}{K}\right)^{\frac{1}{n}} = SA^{\frac{m}{n}} \tag{5}$$

and

$$\chi = \int_{x_b}^{x} \left(\frac{A_0}{A(x)}\right)^{\frac{m}{n}} dx \tag{6}$$

where k_{sn} is the normalized steepness index (Wobus et al., 2006), χ is an integral function of position in the channel network (Perron and Royden, 2013), and A_0 is an arbitrary scaling area, to make the integrand dimensionless. The χ-plot is widely used to analyze the equilibrium of fluvial systems (e.g., Willett et al., 2014; Beeson et al., 2017; Whipple et al., 2017).

We rewrite Eqs. (4 & 5):

$$E = K \cdot {k_{sn}}^{n} = K \cdot \left(\frac{z(x)-z_b}{(A_0)^{\frac{-m}{n}}\chi}\right)^{n}. \tag{7}$$

Based on Eq. (7), the normalized difference in erosion rate across the divide is expressed as a function of K, χ, and n:

$$\frac{\Delta E}{\bar{E}} = \frac{E_\alpha - E_\beta}{(E_\alpha + E_\beta)/2} = 2 \cdot \frac{K_\alpha/K_\beta - (\chi_\alpha/\chi_\beta)^n}{K_\alpha/K_\beta + (\chi_\alpha/\chi_\beta)^n} \tag{8}$$

where E_α is the average erosion rate on the α side, E_β is the average erosion rate on the β side, ΔE is the cross-divide difference in erosion rate ($\Delta E = E_\alpha - E_\beta$), $\bar{E}$ is the average erosion rate across the divide ($\bar{E} = (E_\alpha + E_\beta)/2$), and subscripts α and β denote the two rivers across a divide, assuming that n, A_0, and z_b are uniform across the divide. We plot six curves to illustrate the relationship between the normalized difference in erosion rate ($\Delta E/\bar{E}$) and χ ratio (χ_α/χ_β) under varying n and K_α/K_β values (Fig. 1). It should be noted that the χ_α and χ_β are not the χ values at a reference area as used by Forte and Whipple (2018), but at a same elevation, in which the reciprocal of χ is proportional to k_{sn}. Also, the assignment of the α and the β side can be arbitrary.

In a simplified scenario, a drainage divide moves a horizontal distance of dx_d over a small time interval dt due to cross-divide difference in elevation change, which, in most cases, is driven by the cross-divide differential erosion (Fig. 2). A simple geometric relationship exists (Beeson et al., 2017; Hu et al., 2021):

$$L_{bd} = L_{ad} - L_{ab} = (E_\alpha - U_\alpha)dt - \left(E_\beta - U_\beta\right)dt = (\Delta E - \Delta U)dt \qquad (9)$$

and,

$$L_{bd} = L_{bc} + L_{cd} = dx_d(tan\beta + tan\alpha) \qquad (10)$$

where L denotes length between two points, t is time, α and β are the slope angles on opposite sides of the divide, U_α is average rock uplift rate on the α side, U_β is average rock uplift rate on the β side, and ΔU is the cross-divide difference in rock uplift rate ($\Delta U = U_\alpha - U_\beta$). Therefore,

$$D_{mr} = \frac{dx_d}{dt} = \frac{\Delta E - \Delta U}{tan\alpha + tan\beta} \qquad (11)$$

where D_{mr} is the velocity of drainage divide migration.

From Eq. (8), we can obtain the cross-divide difference in erosion rate, ΔE, when we know K_α/K_β, n, χ_α/χ_β, and the erosion rate around the divide ($\bar{E}$, E_α or E_β). Then, with a known or assumed ΔU, we can calculate the rate of divide migration, D_{mr}, by

$$D_{mr} = \frac{\Delta E - \Delta U}{tan\alpha + tan\beta} = \frac{2\bar{E} \cdot \frac{K\alpha/K_{\beta} - (\chi\alpha/\chi_{\beta})^{n}}{K\alpha/K_{\beta} + (\chi\alpha/\chi_{\beta})^{n}} - \Delta U}{tan\alpha + tan\beta} \tag{12a}$$

$$D_{mr} = \frac{E_{\alpha} \cdot \left[1 - \frac{(\chi\alpha/\chi_{\beta})^{n}}{(K\alpha/K_{\beta})}\right] - \Delta U}{tan\alpha + tan\beta} \tag{12b}$$

or

$$D_{mr} = \frac{E_{\beta} \cdot \left[\frac{(K\alpha/K_{\beta})}{(\chi\alpha/\chi_{\beta})^{n}} - 1\right] - \Delta U}{tan\alpha + tan\beta}. \tag{12c}$$

The detailed derivation process is shown in Supplementary text.

The migration rate can be computed based upon Eq. (12) with the measured or estimated values of E ($\bar{E}$, E_{α} or E_{β}), K_{α}/K_{β}, $\chi_{\alpha}/\chi_{\beta}$, n, ΔU, tanα, and tanβ. The direction of the migration velocity is parallel to the topographic swath profiles and perpendicular to the general trend of the section of the divide.

3. Application in Eastern Tibet

3.1 Background, Tools, and Parameters

Three major rivers, all tributaries of the Yangtze River, flow out of the eastern Tibetan Plateau. They are, from west to east, the Dadu, Min, and Jialing (including Fu) Rivers. We applied the newly derived method to the Dadu-Min and the Min-Jialing drainage divides (Fig. 3 & 4).

To calculate the divide migration rate, we use the Matlab-based toolbox TAK (Forte and Whipple, 2019) and TopoToolbox (Schwanghart and Scherler, 2014) to extract the χ-plot values from ALOS DEM (12.5-m resolution). We obtained the χ-plot with a minimum drainage area of 10^5 m^2 and concavity (m/n) of 0.45 for the drainages close to major divides in eastern Tibet based on the ALOS DEM (12.5-m resolution). We assigned a high base level (e.g., 3500 m in Fig. 5) to achieve top-most linear or quasi-linear χ-plots. We also assigned the eastern side of the divides as the α side. We then calculated χ_α/χ_β and k_{sn} of each side across the divides. We extract topographic swath profiles to calculate the topographic gradients of both sides of the divide ($\tan\alpha$ and $\tan\beta$). For error analysis, we used Oracle Crystal Ball software to carry on Monte Carlo simulation for 10^5 times to determine the 1σ deviation of the migration rates, considering the uncertainties in input parameters (E, K_α/K_β, ΔU, $\tan\alpha$, and $\tan\beta$).

Rocks in the study area can be grouped into three types based on their erodibility: granitoid, sedimentary rock, and Quaternary sediment (Godard et al., 2010). We chose to analyze the channel pairs in the same rock type with similar precipitation to keep similar erosional coefficients across the divide (i.e., $K_\alpha/K_\beta \approx 1$). In addition, n is another required parameter in Eq. (8). We assumed $n = 1$ in the study area, following previous studies (Kirby and Ouimet, 2011; Kirkpatrick et al., 2020). This assumption is comparable with the ^{10}Be-derived data point from the Longmen Shan on the $\Delta E/\bar{E}$ versus χ_α/χ_β diagram, which is plotted near the $n = 1$ curves (Fig. 1).

Both the Dadu-Min and Min-Jialing divides are at high angles (in strike orientation) to the Longmen Shan thrust belt along the plateau margin and the Longriba fault system to the northwest (Fig. 3c). Although the divides are cut by or close to the Minjiang and Maoergai faults, the selection of high base levels places each channel pair in the same block of the faults. As a result, it is most likely that the difference in rock uplift rate (ΔU) is negligible (0 ± 0.10 mm/yr) within a few kilometers across the two major divides.

Several groups have presented lot of ^{10}Be-derived erosion rates in the study area (Fig. 3c). All the elevation of ^{10}Be sample sites are lower than the base level for top-most χ-plots. The ^{10}Be-derived erosion rate, therefore, cover larger area than the top-most χ-plots. Nevertheless, nine ^{10}Be-derived erosion rates (marked as underlined numbers in Fig. 3c) are used as $\bar{E}$, E_α, or E_β for the migration rates calculation at 11 divide sites, because they cover relative small area, which has linear or quasi-linear χ-plots (above the knickpoint) (Fig. 6a, c, & d). For the other sites with no selected ^{10}Be data on any side, we assumed an estimated $\bar{E}$ (0.30 ± 0.10 mm/yr). After measuring the topographic gradient of the two sides on the topographic swath profile, we calculated the divide migration rates using Eq. (12), with the measured or estimated erosion rate ($\bar{E}$, E_α, or E_β). And we also calculated the three other parameters in $\bar{E}$, E_α, E_β, and K, according to the topographic parameters and the input independent parameter (Table 1).

3.2 Results

We calculated 12 and 17 pairs of χ-plots and topographic gradients (tanα and tanβ) across the Dadu-Min and the Min-Jialing divide, respectively, and obtained the migration direction and rate for each (Fig. 4; Table 1). Details of the results are shown in Fig. 5 and Supplementary Materials (Fig. S1-S10).

To examine the influence of the selection of base level, we calculated the χ_α/χ_β

values for a selected profile A-A’ in Fig. 5 across the Min-Jialing divide with 31 base levels varying at an interval of 10 m between 3500 m and 3800 m. The result shows that the $\chi_{\alpha}/\chi_{\beta}$ values are relatively invariant (0.40 ± 0.01) for a base level between 3500 m and 3770 m (Fig. 7), indicating that our calculation is not sensitive to the change of base level, as long as it is high enough. Therefore, we chose a base level of 3500 m to keep a minimal longitudinal length of ~2 km in the four pairs of rivers (Fig. 5). For other river pairs across these two drainage divides, the picked base level elevation ranges from 1700 m to 3950 m (Figs. S2-S9); all are sufficiently high to ensure a stable $\chi_{\alpha}/\chi_{\beta}$ value.

Our results show that the divide migration velocity at each site has a westward component (Fig. 4; Table 1). The migration rates of the Min-Jialing drainage divide range from 0.02 to 0.66 mm/yr, and those of the Dadu-Min drainage divide range from 0.04 to 0.54 mm/yr. While the majority of the migration rates are less than 0.3 mm/yr on both drainage divides, higher rates are found in the northernmost portions of both divides. On the Min-Jialing divide, the highest three rates (0.46 ± 0.29, 0.66 ± 0.24, 0.38 ± 0.18 mm/yr) fall in the Min Shan fault block between the Minjiang and the Huya fault. On the Dadu-Min divide, the greatest two migration rates (0.38 ± 0.17 and 0.54 ± 0.36 mm/yr) are located near the southwestern tip of the dextral strike-slip Maoergai fault. The highest migration rates are spatially linked to fault zones.

We also plotted the precipitation and the relief within a 500 m radius along four and five segments of the Dadu-Min and the Min-Jialing drainage divide, respectively. The precipitation is indistinguishable across the divide, which supports the assumption of similar erosional coefficients (i.e., $K_\alpha/K_\beta \approx 1$). The relief on the aggressors' side is either equal to (Figs. S3c, S5c, and S9c) or greater than that on the victims' side (Figs. 5c, S2c, S4c, S6c, S7c, and S8c). Therefore, the overall pattern of the westward divide migration is largely consistent with the cross-divide contrast in relief.

4. Discussion

4.1 Advantage and limitations of the new method

The drainage divide migration is driven by the cross-divide difference in erosion (Willett et al., 2014; Beeson et al., 2017; Whipple et al., 2017; Hu et al., 2021). Willett et al. (2014) proposed the cross-divide difference in χ as a proxy for the basin disequilibrium. Whipple et al. (2017) and Forte and Whipple (2018) proposed the Gilbert metrics to judge the divide stability. We adopted the cross-divide contrast of the χ-plot with a high base level to calculate the velocity of drainage divide migration in this study. Its essence is the cross-divide difference in k_{sn} (Eq. (7)), which could be treated as a Gilbert metric (Whipple et al., 2017; Forte and Whipple, 2018).

The cross-divide difference in k_{sn} is regarded to be effective to judge divide stability but often cannot be measured in the immediate vicinity of the divide (Whipple et al., 2017). Indeed, k_{sn} does not apply to the headwater hillslope region (between the divide and channel head, where the river system initiates). The comparison of erosion rate in this study, therefore, is not immediately across the divide, but a segment just below the channel head (called “channel head segment” hereinafter). The drainage divide migration is directly driven by the differential erosion of the headwater hillslope regions across the divide, mainly via collapse and landslide (Dahlquist et al., 2018). However, under normal circumstances, the erosion rate in the headwater hillslope region on each side can be considered equal to that at the channel head segment. The migration rate in this study, therefore, shall be regarded as an instantaneous rate in most cases. Even if the erosion rate varies from the headwater hillslope region to the channel head segment, the migration rate calculated by our method could be treated as a quasi-instantaneous rate.

To further validate our method, we chose a lower base level (800 m) and created the χ-plots for six pairs of rivers in eastern Tibet across the Dadu-Min, the Min-Jialing, and the Anning-Dadu drainage divides (Fig. 6a-f). A crossover appears in the χ-plots of four pairs of the aggressor and victim rivers at an elevation between 1.5 and 3.5 km (Fig. 6a-c & f). Rivers 8 and 10 are aggressors, in spite of their relatively high χ value (Fig. 6d & e), which often occur in the case of asymmetric uplift mountain belt (e.g., Fig. 6b in Whipple et al., 2017). Therefore, for a low base level, the cross-divide contrast of channel-head χ values can sometimes fail to reflect the instantaneous migration of drainage divide (Fig. 6a-f).

We suggest that the stability of the drainage divide is only controlled by the gradient at the top of the elevation-χ curve. We use three diagrams to illustrate this argument (Fig. 6g-i). When a disturbance, such as asymmetric uplift, occurs, the drainage system loses its stability, and the divide begins to migrate (Fig. 6g). The aggressor river has a higher χ than the victim river if a low base level at z_{b1} is used (Fig. 6h). In contrast, for a high base level at z_{b2}, the aggressor river yields a lower χ than the victim river (Fig. 6i). One can identify the aggressor and the victim rivers correctly only in the latter case. This highlights the necessity of choosing a high base level in the χ-plot method for the analysis of drainage divide migration.

All methods that judge drainage divide stability, including ours, could be disturbed by variations in erosion coefficient (K, including lithology and precipitation) or asymmetric uplift (Forte and Whipple, 2018; He et al., 2019; Shi et al., 2021). For instance, (1) different K may cause different headwater hillslope gradient and different channel elevation at a reference drainage area across the divide, even if the drainage divide is actually in equilibrium; (2) the divide migration rate in this study could be underestimated or overestimated in the situation of an east- or westward tilt, respectively. Therefore, we chose the sites with similar lithology, precipitation, and uplift rate across the divide when comparing the cross-divide differences in each geomorphic parameter to judge the divide stability. Nevertheless, if the spatial variations in erosion coefficient (K) and uplift rate (U) are known, one can quantitatively assess their influences on the migration of the drainage divide, according to Eq. (12).

The erosion rate, E ($\bar{E}$, E_α, or E_β), is usually unknown, which is a major limitation of this method. If the exact K values are constrained, one can calculate the erosion rate of each side (E_α and E_β) from k_{sn} and K values (Eq. (7); Kirby et al., 2001; Duvall et al., 2004; DiBiase et al., 2018; Ma et al., 2020), and then the migration rate can be obtained by Eq. (11). In principle, one of these four parameters on erosion ($\bar{E}$, E_α, E_β, or K, measured by ^{10}Be or other independent methods) is required in the calculation of divide migration rate, and the rest three parameters can be calculated from the topographic parameters (k_{sn} and χ) (Table 1). If all the four parameters on erosion are unknown, one could use an estimated $\bar{E}$ or K, based on the regional average erosion rate derived from ^{10}Be and other methods (Fig. 3c; Table 1). In this case, using an estimated $\bar{E}$ is preferred, because the K value, affected by the lithology, precipitation, and distance to the active fault, usually has a large variation (Kirkpatrick et al., 2020; Zondervan et al., 2020), whereas the $\bar{E}$ value is relatively less variable.

In general, the migration rate calculation needs parameters of E ($\bar{E}$, E_α or E_β), K_α/K_β, χ_α/χ_β, n, ΔU, tanα, and tanβ. Among these parameters, χ_α/χ_β, tanα, and tanβ are derived from DEM, which have few errors. The others (E, K_α/K_β, n, and ΔU) are inputted parameters based on the actual situation or other independent methods, which may bring uncertainties to the divide migration rate. Although the calculation of divide migration rate in this study may have great uncertainty (Table 1; Fig. S10), we can acquire more accurate divide migration rates with the improvement of accuracy on these inputted parameters.

4.2 Drainage evolution in eastern Tibet and its tectonic implications

A drainage divide in a symmetrical mountain tends to migrate to the side with a greater uplift rate or lower erosion coefficient (stronger lithology or lower precipitation) (Goren et al., 2014; Shi et al., 2021). Figure 8 shows conceptually how disturbance by tectonic strain, lithology, and climate, respectively, can cause the drainage divide migration.

In the eastern Tibetan Plateau, great rivers mainly flowed southeastward during the early Cenozoic (Clark et al., 2004). Following the Cenozoic India-Asia collision, surface uplift of the Tibetan Plateau changed the regional slope trend, causing a reorganization of the drainage system in eastern Tibet (Clark et al., 2004; Zhang et al., 2014; Yang et al., 2020). All Cenozoic great capture events in eastern Tibet show a pattern of which the drainage on the east invaded the one on the west (Fig. 3a). Our results reveal that the Dadu-Min and the Min-Jialing drainage divides both migrated westward at present, which is spatially consistent with the general trend of the great capture events in geological history. Moreover, our results are consistent with previous research on thermochronology and cosmogenic ^{10}Be dating, which suggested the westward regressive erosion in response to a pulse of uplift (since ~10 Ma) along the eastern margin of the Tibetan Plateau (Godard et al., 2010; Tian et al., 2015; Ansberque et al., 2015, 2018; Wang et al., 2021).

The westward migration of the drainage divides in the eastern Tibetan Plateau is a response to the tectonic, climatic, and lithological disturbance at both the regional and the local scales. The tectonic disturbance is reflected by both surface exhumation and crustal deformation in the study area (Fig. 9). Except for some young ages in the hanging-wall of the reverse faults (e.g., the Wenchuan and the Huya Faults), the apatite fission track ages show generally an increasing trend from west to east, indicating a decreasing trend of uplift rate from west to east in the study area (Fig. 9a). Such an increasing trend of ages is not caused by the variation in the samples' elevation; for instance, samples in the Jialing drainage were collected from the lowest elevations (Figs. 9c & S12). The spatial difference in uplift is also recorded by the χ-plots of the channels with a lower base level (Fig. 6) and the k_{sn} map (Fig. 9a), both of which show all victim drainages have higher k_{sn} in the downstream area than the aggressor drainages do.

Cenozoic thickening and growth of the eastern Tibetan Plateau is associated with both brittle deformation in the upper crust, as demonstrated by thrusts and strike-slip faults and their related folds, and viscous, partially-molten rocks in the mid-to-lower crust, as characterized by the high conductivity, low velocity, seismically anisotropic anomalies under the interior of the plateau (Clark and Royden, 2000; Bai et al., 2010; Bao et al., 2020; Liu et al., 2021). The Moho shallows eastward from nearly 60 km depth under the interior of the Tibetan Plateau to almost 40 km in the Sichuan Basin (Wei et al., 2017; Xu et al., 2018; Tan et al., 2019; Lu et al., 2019). At a finer scale, the Moho is offset by a set of reverse faults (Fig. 9b&d) (Guo et al., 2013). Tan et al. (2019) suggested that the eastward motion of the Tibetan crust drives both thrust faulting in the upper crust and ductile shearing and thickening in the mid-to-lower crust. Crustal deformation in this area, therefore, can cause a gentle, east-dipping tilt on the surface (Fig. 9d). Also, the Cenozoic India-Asia collision and the Pacific subduction and trench retreat have driven widespread crustal extension and subsidence throughout East Asia (Northrup et al., 1995; Yin, 2010; Su et al., 2021), which facilitated the formation and connection of large rivers from the Tibetan Plateau to the East Asian marginal seas (e.g., Clark et al., 2004; Zheng et al., 2013).

Moreover, the Cenozoic uplift and growth of the Tibetan Plateau has influenced the East Asian monsoon and strengthened the precipitation in East Asia (Farnsworth et al., 2021). The precipitation rate decreases from more than 1000 mm/yr in the Sichuan basin to ~700 mm/yr in the interior of eastern Tibet (Fig. 3b). All these processes can further intensify the westward divide migration in eastern Tibet (Fig. 9).

Besides the large-scale tectonic and climatic disturbance in eastern Tibet, local fault activities must have also impacted the drainage reorganization (Ansberque et al., 2015; Yang et al., 2020) by changing (most likely enhancing) the rock erodibility (Kirkpatrick et al., 2020) (Fig. 8b). Ansberque et al. (2015) suggested the activity of the Maoergai fault caused the northwestward expending of the Min drainage basin. Our study reveals that the migration rates of the Dadu-Min divide close to the Maoergai fault are noticeably higher than others on the same divide, implying the localized influence of the Maoergai fault activity on the divide migration. Similarly, the relatively high migration rates on the northern half of the Min-Jialing divide could also be attributed to the activity of the Huya fault (Fig. 4).

In brief, our analysis on the stability of drainage divides in the eastern Tibetan Plateau demonstrates that the drainage systems here are not in equilibrium, and the westward migration of drainage divides is still ongoing. The westward drainage divide migration could be driven by the Cenozoic uplift and growth of the Tibetan Plateau, regional extension and subsidence throughout East Asia, strengthening of precipitation, and local fault activities. How to quantitatively differentiate these factors, however, is beyond the scope of this study, but deserves rigorous analysis in future studies.

5. Conclusions

(1) We have developed a new theoretical relationship between the normalized difference in erosion rate and χ ratio (Eq. (8); Fig. 1). It permits quantification of the velocity (i.e., direction and magnitude) of drainage divide migration from topography. We developed a new workflow to achieve the calculation, based on existing software, including the Matlab-based TAK and TopoToolbox, ArcMap GIS platform, and Oracle Crystal Ball, and publically available ALOS DEM data.

(2) We applied this new method to the drainage systems in eastern Tibet and obtained 29 transient divide migration velocities on the Dadu-Min and the Min-Jialing drainage divides. All drainage divides are migrating westward, and their rates vary between 0.02 and 0.66 mm/yr on the Min-Jialing drainage divide and between 0.04 and 0.54 mm/yr for the Dadu-Min drainage divide.

(3) Our findings are consistent with the past great capture events in the eastern Tibetan Plateau. The drainage systems in eastern Tibet are not in equilibrium, and the westward migration of drainage divides is still ongoing, driven by multiple factors at the regional and local scales.

Declaration of Competing Interest

The authors declare that they have no known competing financial interests or personal relationships that could have influenced this work.

Acknowledgments

This study is supported by the Fundamental Research Funds from the Institute of Geology, China Earthquake Administration (IGCEA2004). YL thanks the Governor's University Research Initiative (GURI) Fund from the State of Texas and the University of Houston awarded to Prof. John Suppe. We thank Drs. Sean Willett, Zhanyu Wei, Feng Shi, and Suoya Fan for helpful suggestions which improved the manuscript. The topography data is from https://search.asf.alaska.edu/. The precipitation data are downloaded from http://worldclim.org. The indices in this paper are calculated through TAK (Forte and Whipple, 2019) and TopoToolbox (Schwanghart and Scherler, 2014) on MATLAB.

References

Ansberque, C., Godard, V., Bellier, O., De Sigoyer, J., Liu-Zeng, J., Xu, X., Ren, Z., Li, Y., Team, A.S.T.E.R., 2015. Denudation pattern across the Longriba fault system and implications for the geomorphological evolution of the eastern Tibetan margin. Geomorphology 246, 542-557. https://doi.org/10.1016/j.geomorph.2015.07.017

Ansberque, C., Godard, V., Bellier, O., de Sigoyer, J., Bernet, M., Stubner, K., Tan, X., Xu, X., Ehlers, T.A., 2018. Differential Exhumation Across the Longriba Fault System: Implications for the Eastern Tibetan Plateau. Tectonics 37, 2017TC004816. http://doi.org/10.1002/2017TC004816

Beeson, H.W., McCoy, S.W., Keen-Zebert, A., 2017. Geometric disequilibrium of river basins produces long-lived transient landscapes. Earth Planet. Sci. Lett. 475, 34-43. https://doi.org/10.1016/j.epsl.2017.07.010

Bai, D., Unsworth, M.J., Meju, M.A., Ma, X., Teng, J., Kong, X., Sun, Y., Sun, J., Wang, L., Jiang, C., Zhao, C., 2010. Crustal deformation of the eastern Tibetan plateau revealed by magnetotelluric imaging. Nat. Geosci. 3(5), 358-362. https://doi.org/10.1038/ngeo830

Bao, X., Song, X., Eaton, D.W., Xu, Y., Chen, H., 2020. Episodic lithospheric deformation in eastern Tibet inferred from seismic anisotropy. Geophys. Res. Lett. 47(3), e2019GL085721. https://doi.org/10.1029/2019GL085721

Clark, M.K., Royden, L.H., 2000. Topographic ooze: Building the eastern margin of Tibet by lower crustal flow. Geology 28(8), 703-706. https://doi.org/10.1130/0091-7613(2000)28<703:TOBTEM>2.0.CO;2

Clark, M.K., Schoenbohm, L.M., Royden, L.H., Whipple, K.X., Burchfiel, B.C., Zhang, X., Tang, W., Wang, E., Chen, L., 2004. Surface uplift, tectonics, and erosion of eastern Tibet from large-scale drainage patterns. Tectonics 23, 1-20. https://doi.org/10.1029/2002TC001402

Clark, M.K., House, M.A., Royden, L.H., Whipple, K.X., Burchfiel, B.C., Zhang, X., Tang, W., 2005. Late Cenozoic uplift of southeastern Tibet. Geology 33 (6), 525-528. https://doi.org/10.1130/G21265.1

Dahlquist, M.P., West, A.J., and Li, G., 2018. Landslide-driven drainage divide migration. Geology, https://doi.org/10.1130/G39916.1

DiBiase, R.A., Rossi, M.W. and Neely, A.B., 2018. Fracture density and grain size controls on the relief structure of bedrock landscapes. Geology, 46(5), 399-402. https://doi.org/10.1130/G40006.1

Duvall, A., Kirby, E. and Burbank, D., 2004. Tectonic and lithologic controls on bedrock channel profiles and processes in coastal California. Journal of Geophysical Research: Earth Surface, 109(F3). https://doi.org/10.1029/2003JF000086

Enkelmann, E., Ratschbacher, L., Jonckheere, R., Nestler, R., Fleischer, M., Gloaguen, R., Hacker, B.R., Zhang, Y.Q. and Ma, Y.S., 2006. Cenozoic exhumation and deformation of northeastern Tibet and the Qinling: Is Tibetan lower crustal flow diverging around the Sichuan Basin? Geol. Soc. Am. Bull. 118 (5-6), 651-671. https://doi.org/10.1130/B25805.1

Farnsworth, A., Lunt, D.J., Robinson, S.A., Valdes, P.J., Roberts, W.H., Clift, P.D., Markwick, P., Su, T., Wrobel, N., Bragg, F. and Kelland, S.J., 2019. Past East Asian monsoon evolution controlled by paleogeography, not CO_2. Science Advances, 5(10), p.eaax1697. https://doi.org/10.1126/sciadv.aax1697

Forte, A.M., Whipple, K.X. and Cowgill, E., 2015. Drainage network reveals patterns and history of active deformation in the eastern Greater Caucasus. Geosphere, 11(5), 1343-1364. https://doi.org/10.1130/GES01121.1

Forte, A.M., Whipple, K.X., 2018. Criteria and tools for determining drainage divide stability. Earth Planet. Sci. Lett. 493, 102–117.

https://doi.org/10.1016/j.epsl.2018.04.026
Forte, A.M., Whipple, K.X., 2019. Short communication: The Topographic Analysis Kit (TAK) for TopoToolbox. Earth Surface Dynamics 7, 87–95. https://doi.org/10.5194/esurf-7-87-2019
Godard, V., Lavé, J., Carcaillet, J., Cattin, R., Bourlès, D., Zhu, J., 2010. Spatial distribution of denudation in Eastern Tibet and regressive erosion of plateau margins. Tectonophysics 491(1-4), 253-274. https://doi.org/10.1016/j.tecto.2009.10.026
Goren, L., Willett, S. D., Herman, F., Braun, J., 2014. Coupled numerical–analytical approach to landscape evolution modeling. Earth Surface Processes and Landforms, 39(4), 522-545. https://doi.org/10.1002/esp.3514
Guo, X., Gao, R., Keller, G.R., Xu, X., Wang, H., Li, W., 2013. Imaging the crustal structure beneath the eastern Tibetan Plateau and implications for the uplift of the Longmen Shan range. Earth Planet. Sci. Lett. 379, 72-80. https://doi.org/10.1016/j.epsl.2013.08.005
He, C., Rao, G., Yang, R., Hu, J., Yao, Q., Yang, C.J., 2019. Divide migration in response to asymmetric uplift: Insights from the Wula Shan horst, North China. Geomorphology, 339, 44-57. https://doi.org/10.1016/j.geomorph.2019.04.024
Howard, A.D., 1994, A detachment-limited model of drainage basin evolution: Water Resources Research, 30, 2261–2285. https://doi.org/10.1029/94WR00757
Hu, K., Fang, X., Ferrier, K.L., Granger, D.E., Zhao, Z., Ruetenik, G.A., 2021. Covariation of cross-divide differences in denudation rate and χ: Implications for drainage basin reorganization in the Qilian Shan, northeast Tibet. Earth Planet. Sci. Lett. 562, 116812. https://doi.org/10.1016/j.epsl.2021.116812
Kirby, E., Ouimet, W., 2011. Tectonic geomorphology along the eastern margin of Tibet: Insights into the pattern and processes of active deformation adjacent to the Sichuan Basin. Geol. Soc. London Sp. Pub. 353(1), 165-188. https://doi.org/10.1144/SP353.9
Kirby, E., Whipple, K., 2001. Quantifying differential rock-uplift rates via stream profile analysis. Geology 29(5), 415-418. https://doi.org/10.1130/0091-7613(2001)029<0415:QDRURV>2.0.CO;2
Kirby, E., Whipple, K.X., 2012. Expression of active tectonics in erosional landscapes. J. Struct. Geol. 44, 54-75. https://doi.org/10.1016/j.jsg.2012.07.009
Kirby, E., Whipple, K.X., Tang, W., Chen, Z., 2003. Distribution of active rock uplift along the eastern margin of the Tibetan Plateau: Inferences from bedrock channel longitudinal profiles. J. Geophys. Res.: Solid Earth 108(B4), 1-16. https://doi.org/10.1029/2001JB000861
Kirkpatrick, H.M., Moon, S., Yin, A., Harrison, T.M., 2020. Impact of fault damage on eastern Tibet topography. Geology 49, 30-34. https://doi.org/10.1130/G48179.1
Liang, S., Gan, W., Shen, C., Xiao, G., Liu, J., Chen, W., Ding, X., Zhou, D., 2013. Three- dimensional velocity field of present- day crustal motion of the Tibetan Plateau derived from GPS measurements. J. Geophys. Res.: Solid Earth 118(10),

5722-5732. https://doi.org/10.1002/2013JB010503

Liu, Y., Tan, X., Ye, Y., Zhou, C., Lu, R., Murphy, M.A., Xu, X., Suppe, J., 2020. Role of erosion in creating thrust recesses in a critical-taper wedge: An example from Eastern Tibet. Earth Planet. Sci. Lett. 540, 116270. https://doi.org/10.1016/j.epsl.2020.116270

Liu, Y., Li, L., van Wijk, J.W., Li, A., Fu, Y.V., 2021. Surface wave tomography of the Emeishan large igneous province: Magma storage system, hidden hotspot track, and its impact on the Capitanian mass extinction. Geology. https://doi.org/10.1130/G49055.1

Lu, R., Liu, Y., Xu, X., Tan, X., He, D., Yu, G., Cai, M., and Wu, X., 2019. Three-dimensional model of the lithospheric structure under the eastern Tibetan Plateau: Implications for the active tectonics and seismic hazards. Tectonics 38(4), 1292-1307. https://doi.org/10.1029/2018TC005239

Ma, Z., Zhang, H., Wang, Y., Tao, Y. and Li, X., 2020. Inversion of Dadu River bedrock channels for the late cenozoic uplift history of the eastern Tibetan Plateau. Geophysical Research Letters, 47(4), p.e2019GL086882. https://doi.org/10.1029/2019GL086882

Molnar, P., England, P., 1990. Late Cenozoic uplift of mountain ranges and global climate change: chicken or egg? Nature 346(6279), 29-34. https://doi.org/10.1038/346029a0

Nie, J., Ruetenik, G., Gallagher, K., Hoke, G., Garzione, C.N., Wang, W., Stockli, D., Hu, X., Wang, Z., Wang, Y. and Stevens, T., 2018, Rapid incision of the Mekong River in the middle Miocene linked to monsoonal precipitation: Nature Geoscience, 11(12), 944-948. https://doi.org/10.1038/s41561-018-0244-z

Northrup, C.J., Royden, L.H. and Burchfiel, B.C., 1995. Motion of the Pacific plate relative to Eurasia and its potential relation to Cenozoic extension along the eastern margin of Eurasia. Geology, 23(8), 719-722. https://doi.org/10.1130/0091-7613(1995)023<0719:MOTPPR>2.3.CO;2

Perron, J.T., Royden, L., 2013. An integral approach to bedrock river profile analysis. Earth Surface Processes and Landforms 38(6), 570-576. http://dx.doi.org/10.1002/esp.3302

Rahbek, C., Borregaard, M.K., Antonelli, A., Colwell, R.K., Holt, B.G., Nogues-Bravo, D., Rasmussen, C.M., Richardson, K., Rosing, M.T., Whittaker, R.J. and Fjeldså, J., 2019. Building mountain biodiversity: Geological and evolutionary processes. Science, 365(6458), 1114-1119. https://www.doi.org/10.1126/science.aax0151

Scherler, D., Schwanghart, W., 2020. Drainage divide networks – Part 2: Response to perturbations. Earth Surface Dynamics 8(2), 261-274. https://doi.org/10.5194/esurf-8-261-2020

Schwanghart, W., Scherler, D., 2014. Short Communication: TopoToolbox 2 – MATLAB-based software for topographic analysis and modeling in Earth surface sciences. Earth Surface Dynamics 2 (1), 1-7. https://doi.org/10.5194/esurf-2-1-2014

Shi, F., Tan, X., Zhou, C., Liu, Y., 2021. Impact of asymmetric uplift on mountain asymmetry: Analytical solution, numerical modeling, and natural examples. Geomorphology, 107862. https://doi.org/10.1016/j.geomorph.2021.107862

Steer, P., Simoes, M., Cattin, R., Shyu, J.B.H., 2014. Erosion influences the seismicity of active thrust faults. Nature Communications, 5, 5564. https://doi.org/10.1038/ncomms6564

Su, P., He, H., Tan, X., Liu, Y., Shi, F., Kirby, E., 2021. Initiation and evolution of the Shanxi Rift System in North China: Evidence from low- temperature thermochronology in a plate reconstruction framework. Tectonics, e2020TC006298. https://doi.org/10.1029/2020TC006298

Tan, X.B., Lee, Y.H., Chen, W.Y., Cook, K.L., Xu, X.W., 2014. Exhumation history and faulting activity of the southern segment of the Longmen Shan, eastern Tibet. J. Asian Earth Sci. 81, 91-104. https://doi.org/10.1016/j.jseaes.2013.12.002

Tan, X.B., Lee, Y. H., Xu, X.W., Cook, K.L., 2017a. Cenozoic exhumation of the Danba antiform, eastern Tibet: Evidence from low-temperature thermochronology. Lithosphere 9(4), 534-544. https://doi.org/10.1130/L613.1

Tan, X.B., Xu, X.W., Lee, Y.H., Lu, R.Q., Liu, Y., Xu, C., Li, K., Yu, G.H., Kang, W.J., 2017b. Late Cenozoic thrusting of major faults along the central segment of Longmen Shan, eastern Tibet: Evidence from low-temperature thermochronology. Tectonophysics 712, 145-155. https://doi.org/10.1016/j.tecto.2017.05.016

Tan, X., Yue, H., Liu, Y., Xu, X., Shi, F., Xu, C., Ren, Z., Shyu, J.B.H., Lu, R. and Hao, H., 2018. Topographic loads modified by fluvial incision impact fault activity in the Longmenshan thrust belt, eastern margin of the Tibetan Plateau. Tectonics 37(9), 3001-3017. https://doi.org/10.1029/2017TC004864

Tan, X., Liu, Y., Lee, Y.H., Lu, R., Xu, X., Suppe, J., Shi, F., Xu, C., 2019. Parallelism between the maximum exhumation belt and the Moho ramp along the eastern Tibetan Plateau margin: Coincidence or consequence?. Earth Planet. Sci. Lett. 507, 73-84. https://doi.org/10.1016/j.epsl.2018.12.001

Tian, Y., Kohn, B.P., Hu, S., Gleadow, A.J., 2015. Synchronous fluvial response to surface uplift in the eastern Tibetan Plateau: Implications for crustal dynamics. Geophys. Res. Lett. 42(1), 29-35. https://doi.org/10.1002/2014GL062383

Tian, Y., Li, R., Tang, Y., Xu, X., Wang, Y., Zhang, P., 2018. Thermochronological constraints on the late Cenozoic morphotectonic evolution of the Min Shan, the eastern margin of the Tibetan Plateau. Tectonics 37(6), 1733-1749. https://doi.org/10.1029/2017TC004868

Tucker, G.E., Slingerland, R., 1997. Drainage basin responses to climate change. Water Resources Research, 33 (8), 2031-2047. https://doi.org/10.1029/97WR00409

Vacherat, A., Bonnet, S., Mouthereau, F., 2018. Drainage reorganization and divide migration induced by the excavation of the Ebro basin (NE Spain). Earth Surface Dynamics 6 (2), 369-387. https://doi.org/10.5194/esurf-6-369-2018

Wang, E., Kirby, E., Furlong, K.P., Van Soest, M., Xu, G., Shi, X., Kamp, P.J., Hodges, K.V., 2012. Two-phase growth of high topography in eastern Tibet during the Cenozoic. Nat. Geosci. 5(9), 640-645.

https://doi.org/10.1038/ngeo1538

Wang, W., Godard, V., Liu- Zeng, J., Zhang, J., Li, Z., Xu, S., Yao, W., Yuan, Z., Aumaître, G., Bourlès, D.L., and Keddadouche, K., 2021. Tectonic controls on surface erosion rates in the Longmen Shan, Eastern Tibet. Tectonics, e2020TC006445. https://doi.org/10.1029/2020TC006445

Wei, X., Jiang, M., Liang, X., Chen, L., Ai, Y., 2017. Limited southward underthrusting of the Asian lithosphere and material extrusion beneath the northeastern margin of Tibet, inferred from teleseismic Rayleigh wave tomography. J. Geophys. Res.: Solid Earth, 122, 7172-7189. https://doi.org/10.1002/2016JB013832

Whipple, K.X., Tucker, G.E., 1999. Dynamics of the stream-power river incision model: Implications for height limits of mountain ranges, landscape response timescales, and research needs. J. Geophys. Res., Solid Earth 104 (B8), 17661-17674. https://doi.org/10.1029/1999JB900120

Whipple, K.X., 2009. The influence of climate on the tectonic evolution of mountain belts. Nat. Geosci. 2 (2), 97-104. https://doi.org/10.1038/ngeo413

Whipple, K.X., Forte, A.M., DiBiase, R.A., Gasparini, N.M., Ouimet, W.B., 2017. Timescales of landscape response to divide migration and drainage capture: Implications for the role of divide mobility in landscape evolution. J. Geophys. Res., Earth Surface, 122 (1), 248-273. https://doi.org/10.1002/2016JF003973

Willett, S.D., McCoy, S.W., Perron, J.T., Goren, L., Chen, C.Y., 2014. Dynamic reorganization of river basins. Science 343 (6175), 1117. https://doi.org/10.1126/science.1248765

Wilson, C.J., Fowler, A.P., 2011. Denudational response to surface uplift in east Tibet: Evidence from apatite fission-track thermochronology. Geological Society of America Bulletin 123 (9-10), 1966-1987. https://doi.org/10.1130/B30331.1

Wobus, C., Whipple, K.X., Kirby, E., Snyder, N., Johnson, J., Spyropolou, K., Crosby, B., Sheehan, D., 2006. Tectonics from topography: Procedures, promise, and pitfalls. Geological Society of America Special Papers 398, 55-74. https://doi.org/10.1130/2006.2398(04)

Yang, R., Suhail, H.A., Gourbet, L., Willett, S.D., Fellin, M.G., Lin, X., Gong, J., Wei, X., Maden, C., Jiao, R., Chen, H., 2020. Early Pleistocene drainage pattern changes in Eastern Tibet: Constraints from provenance analysis, thermochronometry, and numerical modeling. Earth Planet. Sci. Lett. 531, 1-10. https://doi.org/10.1073/pnas.1216241110

Yin, A., 2010. Cenozoic tectonic evolution of Asia: A preliminary synthesis. Tectonophysics 488(1-4), 293-325. https://doi.org/10.1016/j.tecto.2009.06.002

Xu, G., Kamp, P.J., 2000. Tectonics and denudation adjacent to the Xianshuihe Fault, eastern Tibetan Plateau: Constraints from fission track thermochronology. J. Geophys. Res., Solid Earth 105 (B8), 19231-19251. https://doi.org/10.1029/2000JB900159

Xu, X., Niu, F., Ding, Z., Chen, Q., 2018. Complicated crustal deformation beneath the NE margin of the Tibetan Plateau and its adjacent areas revealed by multi-station receiver-function gathering. Earth and Planetary Science Letters, 497, 204-216. https://doi.org/10.1016/j.epsl.2018.06.010

Zhang, H., Zhang, P., Champagnac, J.D., Molnar, P., Anderson, R.S., Kirby, E., Craddock, W.H., Liu, S., 2014. Pleistocene drainage reorganization driven by the isostatic response to deep incision into the northeastern Tibetan Plateau. Geology 42 (4), 303-306. https://doi.org/10.1130/G35115.1

Zheng, H., Clift, P.D., Wang, P., Tada, R., Jia, J., He, M., Jourdan, F., 2013. Pre-Miocene birth of the Yangtze River. Proceedings of the National Academy of Sciences 110 (19), 1-6. https://doi.org/10.1073/pnas.1216241110

Zondervan, J.R., Stokes, M., Boulton, S.J., Telfer, M.W., Mather, A.E., 2020. Rock strength and structural controls on fluvial erodibility: Implications for drainage divide mobility in a collisional mountain belt. Earth and Planetary Science Letters 538, 116221. https://doi.org/10.1016/j.epsl.2020.116221

Figure captions

Figure 1. Quantitative relationship between normalized difference in erosion rate and χ ratio across a drainage divide, based on Eq. (8). The relationship is a function of the cross-divide ratio of erosional coefficient (K_α/K_β) and slope exponent (n). Data sources: Ozark Dome from Beeson et al. (2017), Eastern Tibet from Ansberque et al. (2015) and Kirkpatrick et al. (2020).

Figure 2. Schematic illustration in cross-section view for drainage divide migration. The two triangles represent the cross-divide river longitudinal profiles before (dashed) and after (solid) an infinitesimal interval of time (dt). α and β are slopes across the divide; when in subscript, they denote the two rivers across the divide. E is erosion rate, and U is rock uplift rate. dx_d is the horizontal distance of the drainage divide migration, which is the product of drainage divide migration velocity (D_{mr}) and dt. Lowercase letters a-d mark the four points on the auxiliary lines (dotted).

Figure 3. (a) Major drainage systems and the great Cenozoic capture events in the eastern and southeastern Tibetan Plateau. (b) Precipitation distribution in the same region. Precipitation data (1970-2000) are from http://worldclim.org. Inset is a plot of precipitation along a 60-km-wide swath profile P-P'. Black curve indicates the mean precipitation and the grey shade below the curve shows the maximum and minimum

precipitation. (c) Map of published cosmogenic ^{10}Be ages and the derived erosion rates. The underlined numbers and non-transparent coloring indicate the erosion rates and their covering areas that are applied directly in the calculation of divide migration. Others are only applied for the estimation of regional average erosion rate. Data sources: Ouimet et al. (2009), Godard et al. (2010), Ansberque et al. (2015), and Kirkpatrick et al. (2020).

Figure 4. Drainage system in eastern Tibet and the calculated migration velocity of the Dadu-Min and Min-Jialing divides. Dark blue vector indicates the velocity of drainage divide migration. See Table 1 for direction and magnitude. Red curve marks the drainage divide. Thick, translucent curves indicate the channels 1-10 in Fig. 7, whose base level elevations are 800 m.

Figure 5. (a) χ map of a upstream region of the Min and Jialing river drainages, with a uniform base elevation at 3500 m. See Fig. 4 for location. (b) χ-plots for four pairs of rivers across the Min-Jialing drainage divide (left) and their swath profiles of topography (right) along A-A', B-B', C-C', and D-D'. Numbers in the χ-plots are the χ values at the same top-most elevation and the average k_{sn} values (the underlined numbers) in units of $m^{0.9}$. Numbers with no unit in the right panel are the values of $\tan\alpha$ and $\tan\beta$. The velocity of divide migration is labelled on top of the divide. The K value of each site is in units of $10^{-6}m^{0.1}yr^{-1}$. (c) Precipitation (http://worldclim.org) and relief (within 500 m radius) along the drainage divide E-E' (see Fig. 5a for

location). The swath profiles E-E' extends to both sides of the drainage divide by 2 km and 0.5 km for precipitation and relief, respectively.

Figure 6. (a-f) Comparison of χ-plots of six pairs of rivers with a base elevation of 800 m. The locations of channels 1-10 are shown in Fig. 4. Channels 11 and 12 are two rivers in the southeastern Tibet from Yang et al. (2020) and their locations are not shown in this study. Note that: (1) In each diagram, the victim river shows a greater slope of elevation-χ (i.e., higher k_{sn}) than the aggressor river does in the downstream area; in contrast, the victim river has a smaller slope of elevation-χ (i.e., lower k_{sn}) in the upstream area (above the marked knickpoints). (2) Channels 7 and 9 are victims, although they have lower χ values for the full basin than channels 8 and 10 do, respectively. (3) The elevations of base level for the top-most χ-plots, the knickpoints, and four ^{10}Be samples are presented. The elevations of other ^{10}Be samples are shown in Figure S11. (g-i) Schematic diagrams of disequilibrium of drainage systems in response to asymmetric uplift, and its χ-plot with different base levels (z_{b1} and z_{b2}).

Figure 7. A test on the selection and stability of base levels. (a) Varying base level z_b versus its corresponding χ_α/χ_β values. The base level increases from 3500 m to 3800 m at an increment of 10 m. The χ_α/χ_β values fall around 0.4 for base levels

between 3500 and 3770 m. (b) Histogram and frequency distribution of the calculated χ_α/χ_β values for varying base level elevations.

Figure 8. Cartoon diagrams for drainage divide migration caused by tectonic (a), lithological (b), and climatic (c) disturbances, respectively. It should be noted that the divide is in equilibrium before these disturbances, and the diagrams show the initial status after each disturbance.

Figure 9. (a) Topography, normalized channel steepness, major faults, and apatite fission track ages in eastern Tibet. Thick red curves denote the Dadu-Min and the Min-Jialing drainage divides, and black are major faults. Yellow stars show the location and ages of the published apatite fission track samples. References: [1] = Xu and Kamp, 2000; [2] = Wilson and Fowler, 2011; [3] = Tan et al., 2017a; [4] = Clark et al., 2005; [5] = Tan et al., 2014; [6] = Tian et al., 2015; [7] = Tan et al., 2017b; [8] = Wang et al., 2012; [9] = Ansberque et al., 2018; [10] = Tan et al., 2019; [11] = Tian et al., 2018; [12] = Enkelmann et al., 2006. (b) Drainage divides, major faults, and GPS measurements overlying a map of the depth of the Moho. The Moho depth map is generated by Lu et al. (2019) based on Rayleigh wave tomography of Wei et al. (2017). Blue arrows show GPS measurements with 95% confidence interval in the Eurasian reference (from Liang et al., 2013). (c) Distribution of apatite fission track ages and the samples' elevation along the Y-Y' profile. The location of the Y-Y' profile is shown in Fig. 9a. (d) Topography and crustal structure profile X-X′ across

the eastern Tibetan Plateau. Profile location is shown in (a) and largely overlaps the seismic profile of Guo et al. (2013). The precipitation difference is schematically shown as clouds and rains based on the measurements shown in Fig. 3b. Red stars indicate three earthquakes nearby, including, from NW to SE, the 25 Aug 1933 M_s 7.5 Diexi, the 18 July 2008 M_s 5.1, and the 13 May 2008 M_s 5.2 events. Yellow dots indicate the aftershocks of the 12 May 2008 M_w 7.9 Wenchuan earthquake. Abbreviations: Pz-Mz sed, Paleozoic-Mesozoic sedimentary rocks; LRQF, Longriqu Fault; MEGF, Maoergai Fault; MJF, Minjiang Fault; WMF, Wenchuan-Maoxian Fault; BYF, Beichuan-Yingxiu Fault; JGF, Jiangyou-Guanxian Fault. Red, grey, and white arrows are not to scale.

Table 1. Calculation of the velocity of drainage divide migration in eastern Tibet.

Divide Information		Topographic Parameters Extracted from DEM							Parameters on erosion rate (at least 1 of 4 is required)				Drainage Divide Migration	
Site	Location	Base Elev.	Head Elev.	tanα	tanβ	χ_α/χ_β	$k_{sn}(\alpha)$ ($m^{0.9}$)	$k_{sn}(\beta)$ ($m^{0.9}$)	E_α (mm/yr)	E_β (mm/yr)	$\bar{E}$ (mm/yr)	K ($10^{-6}m^{0.1}yr^{-1}$)	Direction	Rate (mm/yr)
Min-Jialing drainage divide														
Fig. 5-A	103.819°E, 33.011°N	3500m	3939m	0.47 ± 0.01	0.30 ± 0.01	2.20/5.73	199.55	76.61	0.43 ± 0.14	0.17 ± 0.06	0.30 ± 0.10	2.17 ± 0.72	276°	0.35 ± 0.12
Fig. 5-B	103.834°E, 32.978°N	3500m	4078m	0.33 ± 0.01	0.27 ± 0.01	4.52/5.68	127.88	101.76	0.30 ± 0.08	0.24±0.06 (1)	0.27 ± 0.07	2.36 ± 0.59	231°	0.10 ± 0.06
Fig. 5-C	103.876°E, 32.937°N	3500m	3936m	0.52 ± 0.01	0.26 ± 0.01	3.48/6.39	125.29	68.23	0.44 ± 0.11	0.24±0.06 (1)	0.34 ± 0.09	3.52 ± 0.88	264°	0.26 ± 0.09
Fig. 5-D	103.890°E, 32.890°N	3500m	4093m	0.22 ± 0.01	0.16 ± 0.01	4.84/7.20	122.52	82.36	0.53 ± 0.08 (1)	0.36 ± 0.05	0.44 ± 0.07	4.33 ± 0.65	304°	0.46 ± 0.29
Fig. S6-A	103.869°E, 31.880°N	1700m	2723m	0.38 ± 0.01	0.42 ± 0.01	6.59/8.56	155.24	119.51	0.34 ± 0.11	0.26 ± 0.09	0.30 ± 0.10	2.18 ± 0.73	234°	0.10 ± 0.14
Fig. S6-B	103.907°E, 31.823°N	1700m	2490m	0.67 ± 0.01	0.50 ± 0.01	4.94/7.20	159.92	109.72	0.36 ± 0.12	0.24 ± 0.08	0.30 ± 0.10	2.23 ± 0.74	224°	0.10 ± 0.09
Fig. S7-A	103.821°E, 32.349°N	2600m	3750m	0.61 ± 0.01	0.73 ± 0.01	5.69/7.36	202.11	156.25	0.34 ± 0.11	0.26 ± 0.09	0.30 ± 0.10	1.67 ± 0.56	313°	0.06 ± 0.08
Fig. S7-B	103.803°E, 32.318°N	2600m	4106m	0.69 ± 0.01	0.76 ± 0.01	7.32/8.10	205.74	185.93	0.61 ± 0.08	0.55±0.077 (2)	0.58 ± 0.08	2.96 ± 0.41	261°	0.04 ± 0.08
Fig. S7-C	103.833°E, 32.182°N	2600m	3361m	0.71 ± 0.01	0.66 ± 0.01	4.15/5.28	183.37	144.13	0.34 ± 0.11	0.26 ± 0.09	0.30 ± 0.10	1.83 ± 0.61	263°	0.05 ± 0.08
Fig. S7-D	103.822°E, 32.071°N	2600m	3577m	0.58 ± 0.01	0.54 ± 0.01	5.35/6.88	182.62	142.01	0.72 ± 0.08	0.56±0.065 (2)	0.64 ± 0.07	3.94 ± 0.46	292°	0.14 ± 0.11
Fig. S8-A	103.819°E, 32.816°N	3500m	3920m	0.27 ± 0.01	0.21 ± 0.01	2.61/6.46	160.92	65.02	0.53 ± 0.08 (1)	0.21 ± 0.03	0.37 ± 0.06	3.29 ± 0.50	267°	0.66 ± 0.24
Fig. S8-B	103.738°E, 32.738°N	3500m	3742m	0.24 ± 0.01	0.36 ± 0.01	1.25/2.30	193.60	105.22	0.51 ± 0.05	0.27 ± 0.03	0.39 ± 0.04	2.61 ± 0.26	255°	0.38 ± 0.18
Fig. S8-C	103.883°E, 32.648°N	3500m	4059m	1.00 ± 0.01	0.75 ± 0.01	2.87/3.83	194.77	145.95	0.34 ± 0.11	0.26 ± 0.09	0.30 ± 0.10	1.76 ± 0.59	236°	0.05 ± 0.02
Fig. S8-D	103.786°E, 32.551°N	3500m	3739m	0.60 ± 0.01	0.51 ± 0.01	0.89/1.91	268.54	125.13	0.41 ± 0.14	0.19 ± 0.06	0.30 ± 0.10	1.52 ± 0.51	259°	0.19 ± 0.07
Fig. S9-A	103.418°E, 33.089°N	3500m	3821m	0.37 ± 0.01	0.37 ± 0.01	7.32/8.15	43.85	39.39	0.16 ± 0.02	0.14 ± 0.015 (2)	0.15 ± 0.02	3.55 ± 0.38	189°	0.02 ± 0.02
Fig. S9-B	103.578°E, 33.135°N	3500m	3797m	0.46 ± 0.01	0.40 ± 0.01	3.21/4.90	92.52	60.61	0.36 ± 0.12	0.24 ± 0.08	0.30 ± 0.10	3.92 ± 0.13	232°	0.14 ± 0.06
Fig. S9-C	103.652°E, 33.120°N	3500m	3692m	0.31 ± 0.01	0.39 ± 0.01	2.09/3.62	91.87	53.04	0.38 ± 0.13	0.22 ± 0.07	0.30 ± 0.10	4.14 ± 0.14	210°	0.23 ± 0.09
Dadu-Min drainage divide														
Fig. S2-A	102.977°E, 31.087°N	3700m	4317m	0.96 ± 0.01	0.52 ± 0.01	3.56/7.13	173.31	86.54	0.40 ± 0.13	0.20 ± 0.07	0.30 ± 0.10	2.31 ± 0.77	252°	0.14 ± 0.08
Fig. S2-B	102.901°E, 30.924°N	3700m	4349m	0.67 ± 0.01	0.62 ± 0.01	4.16/6.30	156.01	103.02	0.36 ± 0.12	0.24 ± 0.08	0.30 ± 0.10	2.32 ± 0.77	259°	0.10 ± 0.09
Fig. S3-A	102.687°E, 31.970°N	3500m	4062m	0.34 ± 0.01	0.55 ± 0.01	3.51/4.58	160.11	122.71	0.38 ± 0.05 (2)	0.29 ± 0.04	0.34 ± 0.04	2.37 ± 0.31	255°	0.10 ± 0.12
Fig. S3-B	102.677°E, 31.859°N	3500m	3998m	0.47 ± 0.01	0.33 ± 0.01	3.19/4.11	156.11	121.17	0.34 ± 0.11	0.26 ± 0.09	0.30 ± 0.10	2.16 ± 0.72	311°	0.09 ± 0.13
Fig. S3-C	102.634°E, 31.672°N	3500m	4599m	0.51 ± 0.01	0.79 ± 0.01	6.58/9.45	167.02	116.30	0.35 ± 0.12	0.25 ± 0.08	0.30 ± 0.10	2.12 ± 0.71	283°	0.08 ± 0.08
Fig. S3-D	102.607°E, 31.628°N	3500m	4311m	0.66 ± 0.01	0.54 ± 0.01	4.49/7.05	180.62	115.04	0.37 ± 0.12	0.23 ± 0.08	0.30 ± 0.10	2.03 ± 0.68	284°	0.11 ± 0.09
Fig. S3-E	102.680°E, 31.485°N	3500m	4413m	0.39 ± 0.01	1.08 ± 0.01	5.69/7.61	160.46	119.97	0.34 ± 0.11	0.26 ± 0.09	0.30 ± 0.10	2.14 ± 0.72	274°	0.06 ± 0.07
Fig. S4-A	102.599°E, 32.221°N	3700m	4033m	0.56 ± 0.01	0.34 ± 0.01	3.36/4.06	99.11	82.02	0.33 ± 0.11	0.27 ± 0.09	0.30 ± 0.10	3.31 ± 0.11	278°	0.06 ± 0.12
Fig. S4-B	102.604°E, 32.184°N	3700m	4186m	0.70 ± 0.01	0.40 ± 0.01	3.94/5.57	123.35	87.25	0.42 ± 0.048 (2)	0.30 ± 0.03	0.34 ± 0.04	3.40 ± 0.39	260°	0.11 ± 0.10
Fig. S4-C	102.628°E, 32.124°N	3700m	4227m	0.65 ± 0.01	0.36 ± 0.01	3.92/4.48	134.44	117.63	0.30 ± 0.04 (2)	0.26 ± 0.03	0.34 ± 0.04	2.23 ± 0.30	222°	0.04 ± 0.10
Fig. S5-A	102.714°E, 32.438°N	3950m	4125m	0.46 ± 0.01	0.40 ± 0.01	0.65/2.16	269.23	81.02	0.46 ± 0.15	0.14 ± 0.05	0.30 ± 0.10	1.71 ± 0.57	288°	0.38 ± 0.17
Fig. S5-B	102.674°E, 32.395°N	3950m	4187m	0.19 ± 0.01	0.14 ± 0.01	1.70/3.14	139.41	75.48	0.39 ± 0.13	0.21 ± 0.07	0.30 ± 0.10	2.79 ± 0.93	255°	0.54 ± 0.36

Notes: The uncertainties of migration rates are 1σ. Estimated values for calculation: $\bar{E}$ = 0.30 ± 0.10 mm/yr, ΔU = 0 ± 0.10 mm/yr, K_α/K_β = 1.0 ± 0.1, and n = 1. The underlined numbers in "Parameters on erosion rate" column indicate the input parameters, and others are computed according to each input parameter.

References: (1) Kirkpatrick et al., 2020. (2) Ansberque et al., 2015.

Figure 1

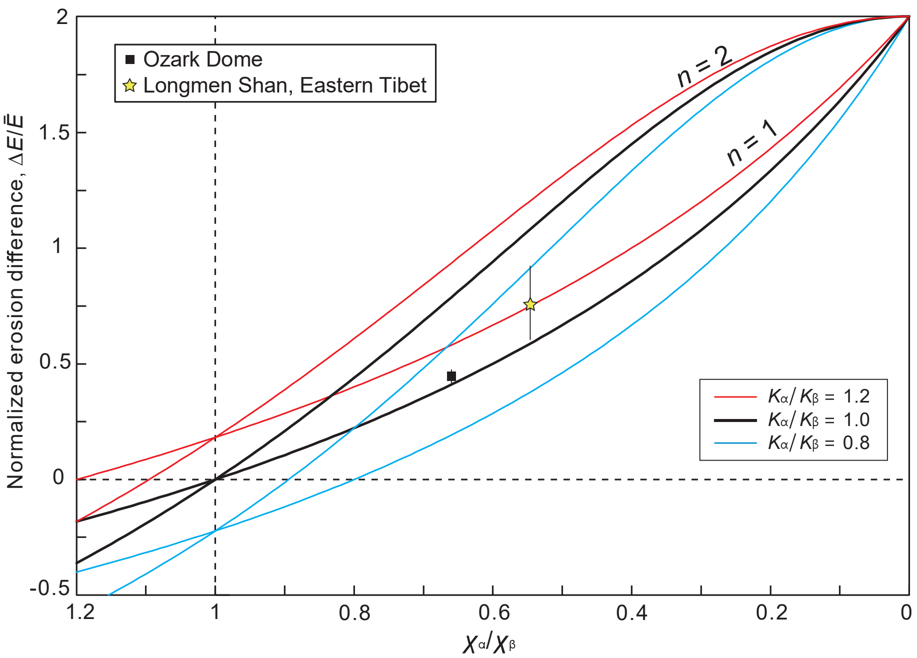

Ozark Dome
Longmen Shan, Eastern Tibet
n = 2
n = 1
Kα/ Kβ = 1.2
Kα/ Kβ = 1.0
Kα/ Kβ = 0.8
Normalized erosion difference, ΔE/Ē
χα/χβ
2
1.5
1
0.5
0
-0.5
1.2
1
0.8
0.6
0.4
0.2
0

Figure 2

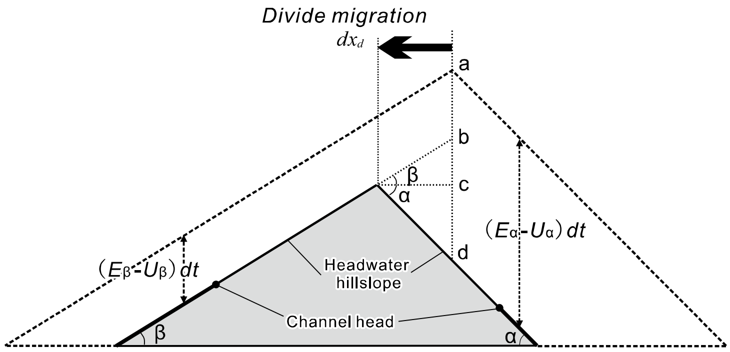

Divide migration
dx_d
a
b
c
d
β
α
$(E_\alpha - U_\alpha)dt$
$(E_\beta - U_\beta)dt$
Headwater
hillslope
Channel head
β
α

Figure 3

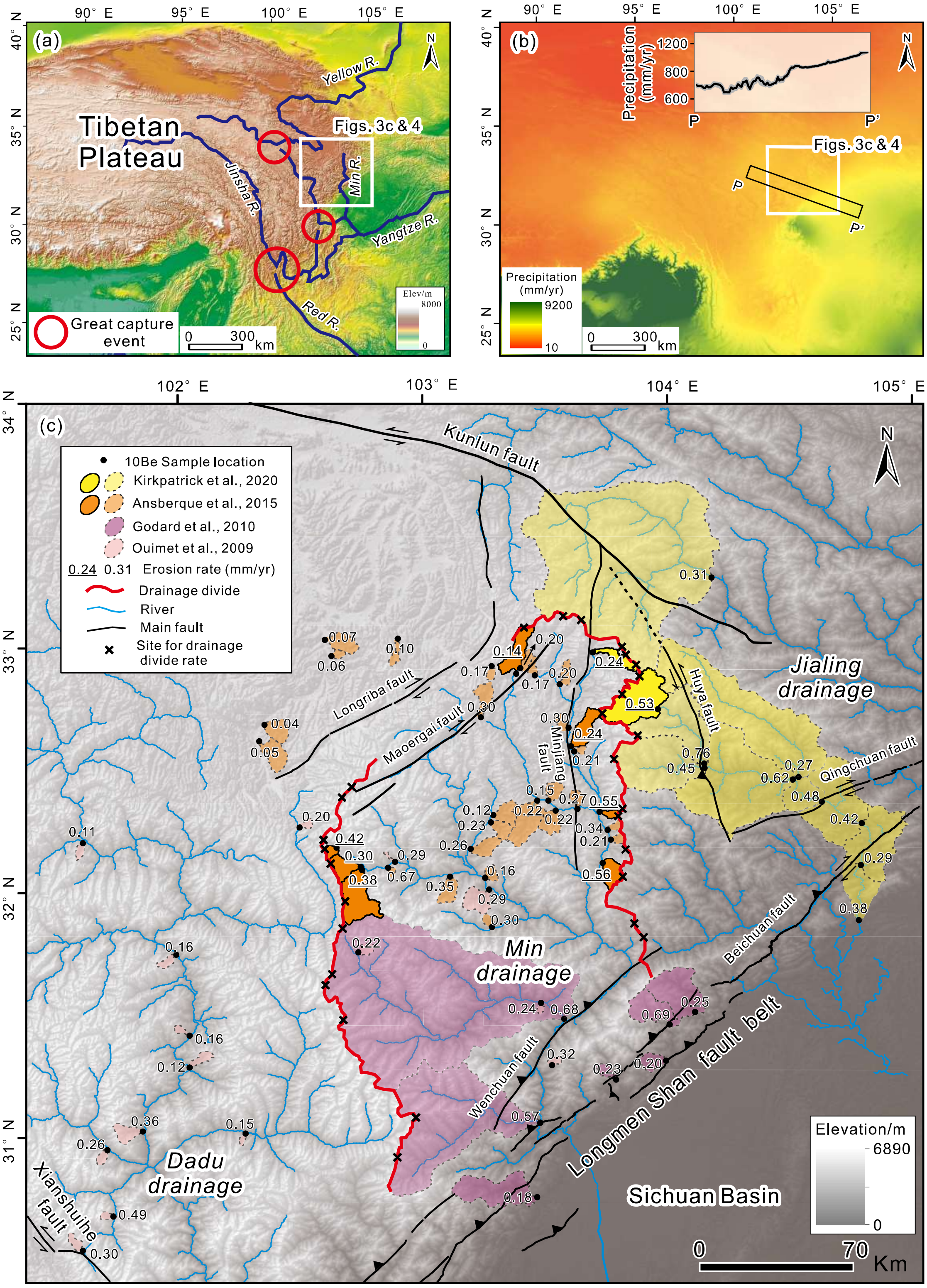

(a)
Tibetan Plateau
Yellow R.
Figs. 3c & 4
Min R.
Jinsha R.
Yangtze R.
Red R.
Great capture event
Elev/m
8000
0
300 km
(b)
Precipitation (mm/yr)
1200
800
600
P
P'
Figs. 3c & 4
9200
10
300 km
(c)
10Be Sample location
Kirkpatrick et al., 2020
Ansberque et al., 2015
Godard et al., 2010
Ouimet et al., 2009
0.24 0.31 Erosion rate (mm/yr)
Drainage divide
River
Main fault
Site for drainage divide rate
Kunlun fault
Longriba fault
Maoergai fault
Minjiang fault
Huya fault
Qingchuan fault
Beichuan fault
Wenchuan fault
Longmen Shan fault belt
Xianshuihe fault
Jialing drainage
Min drainage
Dadu drainage
Sichuan Basin
Elevation/m
6890
0
70 Km

Figure 4

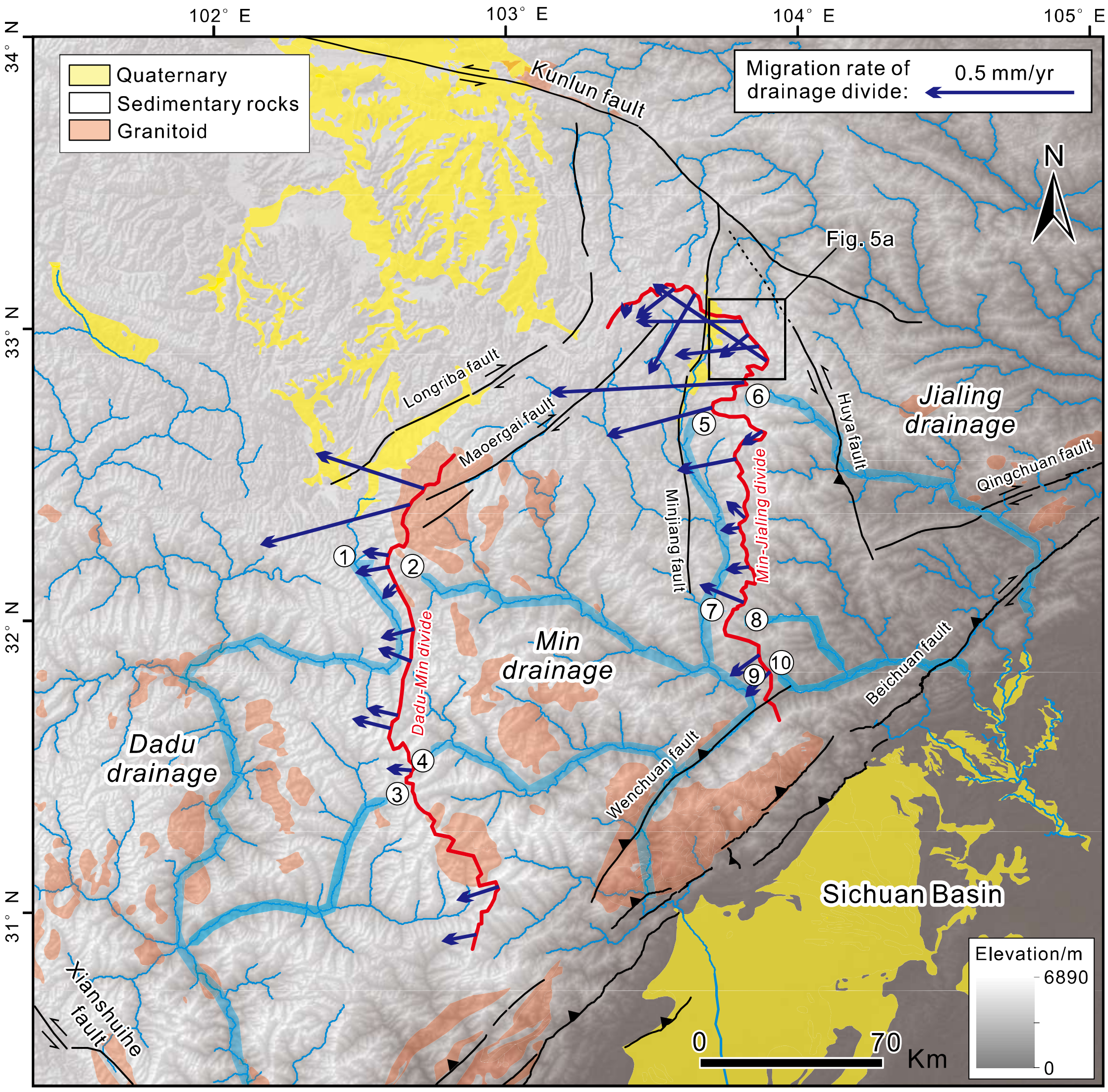

102° E
103° E
104° E
105° E
34° N
33° N
32° N
31° N
Quaternary
Sedimentary rocks
Granitoid
Migration rate of drainage divide:
0.5 mm/yr
N
Kunlun fault
Fig. 5a
Longriba fault
Maoergai fault
Minjiang fault
Min-Jialing divide
Huya fault
Jialing drainage
Qingchuan fault
Dadu-Min divide
Min drainage
Dadu drainage
Beichuan fault
Wenchuan fault
Sichuan Basin
Xianshuihe fault
Elevation/m
6890
0
0
70
Km

Figure 5

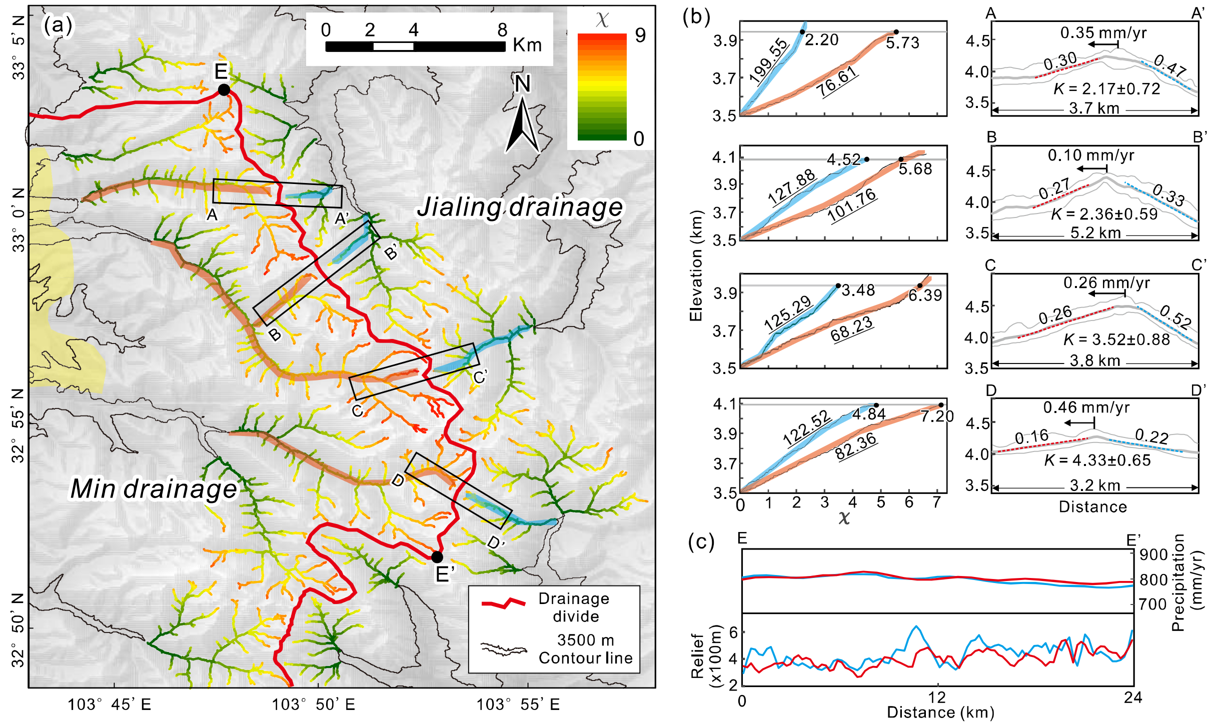

(a)
0 2 4 8 Km
N
χ
9
0
E
E'
A
A'
B
B'
C
C'
D
D'
Jialing drainage
Min drainage
Drainage divide
3500 m Contour line
33° 5' N
33° 0' N
32° 55' N
32° 50' N
103° 45' E
103° 50' E
103° 55' E
(b)
Elevation (km)
χ
199.55
2.20
76.61
5.73
127.88
4.52
101.76
5.68
125.29
3.48
68.23
6.39
122.52
4.84
82.36
7.20
0.35 mm/yr
0.30
0.47
K = 2.17±0.72
3.7 km
0.10 mm/yr
0.27
0.33
K = 2.36±0.59
5.2 km
0.26 mm/yr
0.26
0.52
K = 3.52±0.88
3.8 km
0.46 mm/yr
0.16
0.22
K = 4.33±0.65
3.2 km
Distance
(c)
Precipitation (mm/yr)
Relief (x100m)
Distance (km)

Figure 6

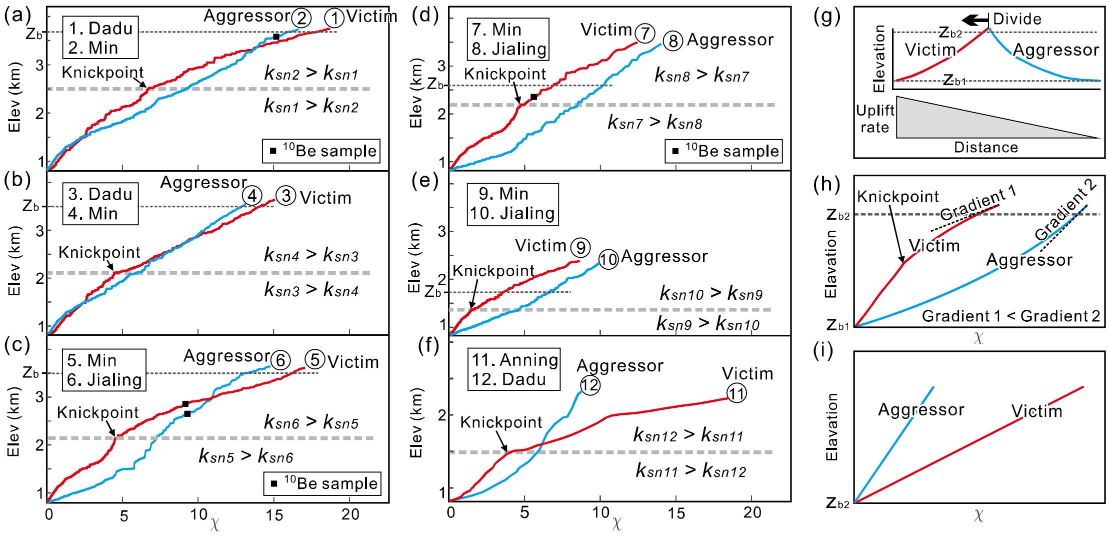

(a)
1. Dadu
2. Min
Aggressor 2
1 Victim
Knickpoint
$k_{sn2} > k_{sn1}$
$k_{sn1} > k_{sn2}$
^{10}Be sample
(b)
3. Dadu
4. Min
Aggressor 4
3 Victim
Knickpoint
$k_{sn4} > k_{sn3}$
$k_{sn3} > k_{sn4}$
(c)
5. Min
6. Jialing
Aggressor 6
5 Victim
Knickpoint
$k_{sn6} > k_{sn5}$
$k_{sn5} > k_{sn6}$
^{10}Be sample
(d)
7. Min
8. Jialing
Victim 7
8 Aggressor
Knickpoint
$k_{sn8} > k_{sn7}$
$k_{sn7} > k_{sn8}$
^{10}Be sample
(e)
9. Min
10. Jialing
Victim 9
10 Aggressor
Knickpoint
$k_{sn10} > k_{sn9}$
$k_{sn9} > k_{sn10}$
(f)
11. Anning
12. Dadu
Aggressor 12
Victim 11
Knickpoint
$k_{sn12} > k_{sn11}$
$k_{sn11} > k_{sn12}$
Elev (km)
Z_b
χ
(g)
Divide
Victim
Aggressor
Z_{b2}
Z_{b1}
Elevation
Uplift rate
Distance
(h)
Knickpoint
Gradient 1
Gradient 2
Victim
Aggressor
Gradient 1 < Gradient 2
Elavation
Z_{b2}
Z_{b1}
χ
(i)
Aggressor
Victim
Elavation
Z_{b2}
χ

Figure 7

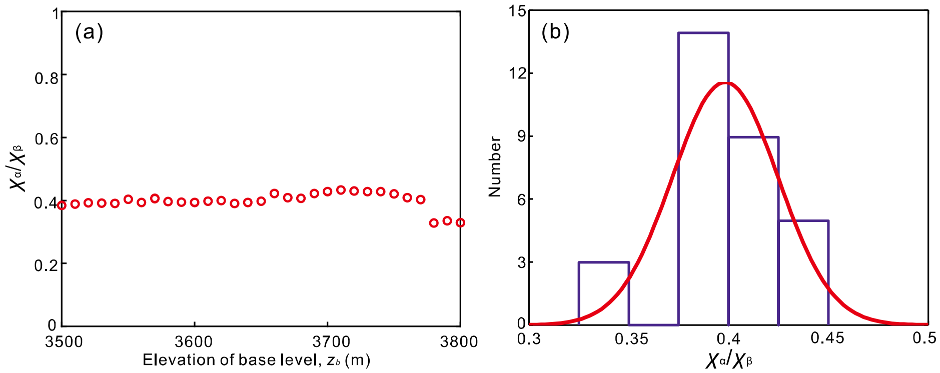

(a)
χ_α/χ_β
Elevation of base level, z_b (m)
0
0.2
0.4
0.6
0.8
1
3500
3600
3700
3800
(b)
Number
χ_α/χ_β
0
3
6
9
12
15
0.3
0.35
0.4
0.45
0.5

Figure 8

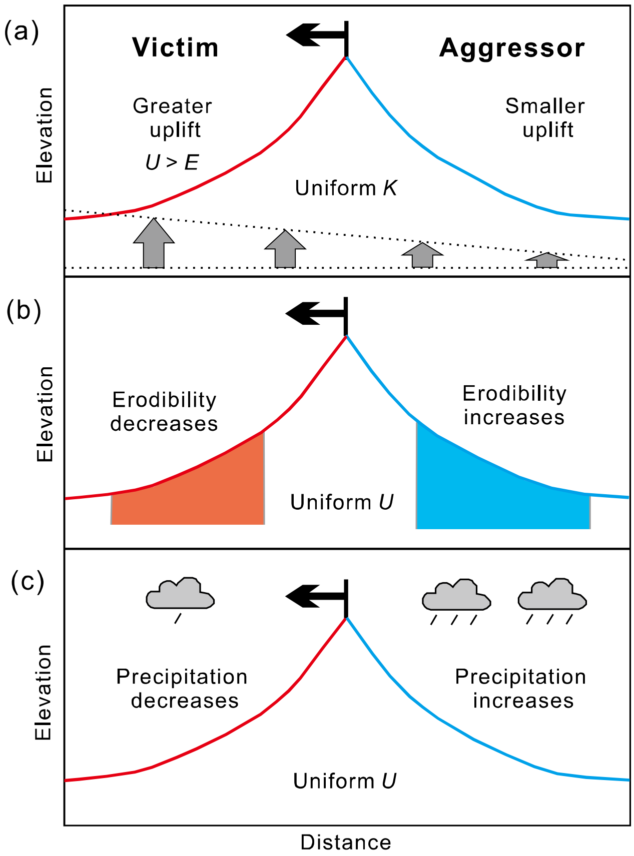

(a)
Victim
Aggressor
Greater
uplift
U > E
Smaller
uplift
Uniform K
Elevation
(b)
Erodibility
decreases
Erodibility
increases
Uniform U
Elevation
(c)
Precipitation
decreases
Precipitation
increases
Uniform U
Elevation
Distance

Figure 9

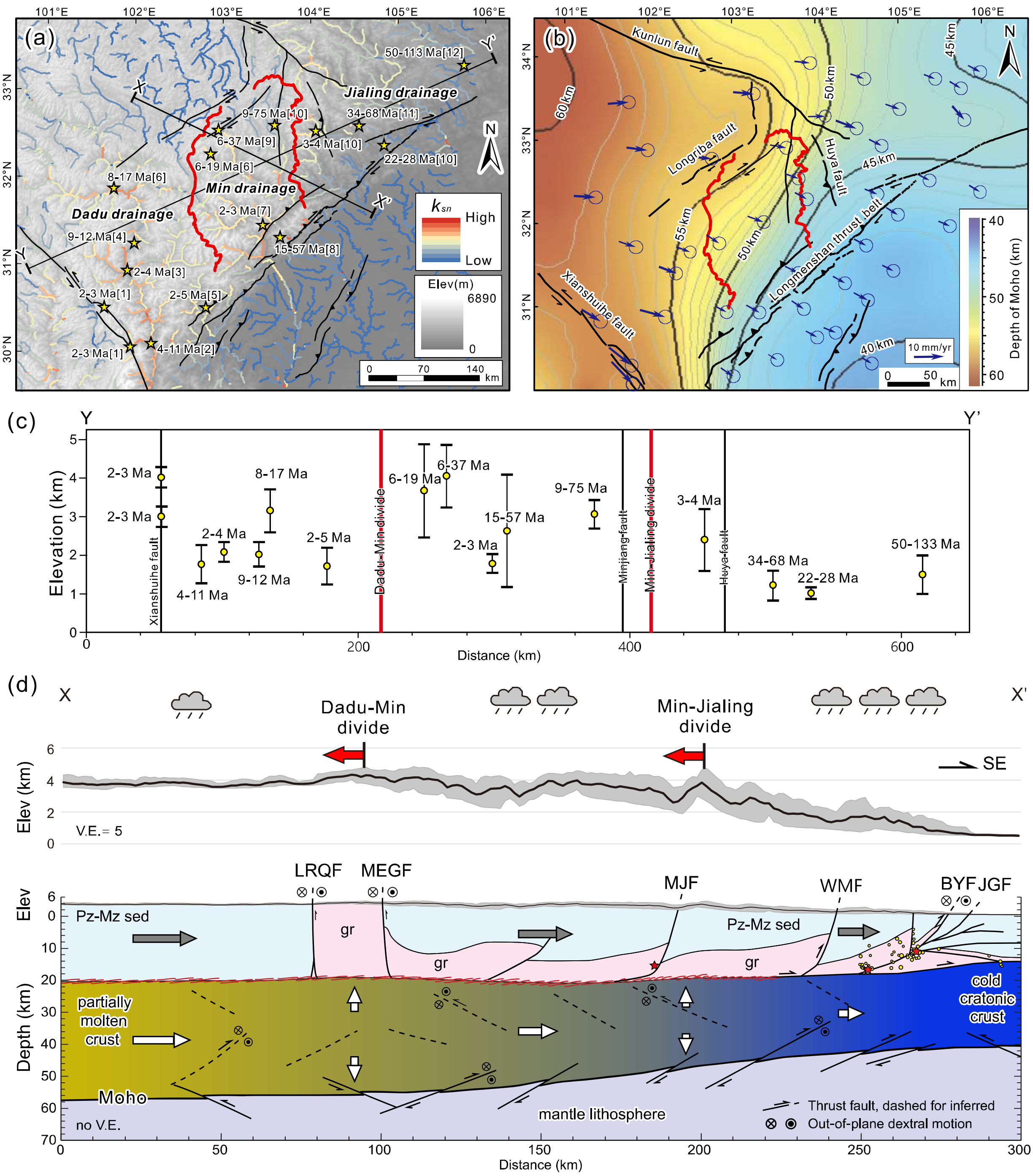

(a)
101°E
102°E
103°E
104°E
105°E
106°E
33°N
32°N
31°N
30°N
50-113 Ma[12]
Jialing drainage
9-75 Ma[10]
34-68 Ma[11]
6-37 Ma[9]
3-4 Ma[10]
6-19 Ma[6]
22-28 Ma[10]
8-17 Ma[6]
Min drainage
Dadu drainage
2-3 Ma[7]
9-12 Ma[4]
15-57 Ma[8]
2-4 Ma[3]
2-3 Ma[1]
2-5 Ma[5]
2-3 Ma[1]
4-11 Ma[2]
X
X'
Y
Y'
N
k_{sn}
High
Low
Elev(m)
6890
0
0
70
140
km
(b)
Kunlun fault
60 km
50 km
45 km
Longriba fault
Huya fault
45 km
55 km
50 km
Longmenshan thrust belt
Xianshuihe fault
40 km
10 mm/yr
0
50
km
40
50
60
Depth of Moho (km)
(c)
Y
Y'
Elevation (km)
Distance (km)
2-3 Ma
2-3 Ma
2-4 Ma
8-17 Ma
4-11 Ma
9-12 Ma
2-5 Ma
6-19 Ma
6-37 Ma
15-57 Ma
2-3 Ma
9-75 Ma
3-4 Ma
34-68 Ma
22-28 Ma
50-133 Ma
Xianshuihe fault
Dadu-Min divide
Minjiang fault
Min-Jialing divide
Huya fault
(d)
X
X'
Dadu-Min
divide
Min-Jialing
divide
SE
Elev (km)
V.E.= 5
LRQF
MEGF
MJF
WMF
BYF
JGF
Elev
Depth (km)
Pz-Mz sed
gr
gr
Pz-Mz sed
gr
partially
molten
crust
cold
cratonic
crust
Moho
mantle lithosphere
no V.E.
Thrust fault, dashed for inferred
Out-of-plane dextral motion
Distance (km)

Click here to access/download
Supplementary material for online publication only
Supplementary material.docx